Transparent Grid Enablement
Using Transparent Shaping and GRID superscalar

S. Masoud Sadjadi, Juan Carlos Martinez, Luis Atencio, and Tatiana Soldo
Autonomic and Grid Computing Research Lab
School of Computing and Information Sciences, FIU
Contact: sadjadi@cs.fiu.edu

Rosa M. Badia and Jorge Ejarque
Grid Computing and Clusters
Barcelona Supercomputing Center and UPC, Spain
Contact: rosa.m.badia@bsc.es

I. Description and Motivation

- **What is the project trying to do?**
  - Explore techniques and tools to simplify the process of grid enablement
- **Why is it important?**
  - Building, debugging, deploying, and maintaining Grid enabled application is difficult (even when a sequential version of the application exists)
- **What is the expected output?**
  - Methodologies and tools that enable easy implementation of Grid applications.
- **Case Study**
  - Matrix Multiplication
  - Hurricane Mitigation Applications

II. Background Information: Transparent Shaping

- Transparent Shaping is a programming model that allows software systems to change their behavior *transparently* at runtime, i.e. without any manual modifications to the original code.
- TRAP/J (Transparent Reflective Aspect Programming in Java) is the realization of this model in Java, which provides dynamic adaptation to existing Java application.

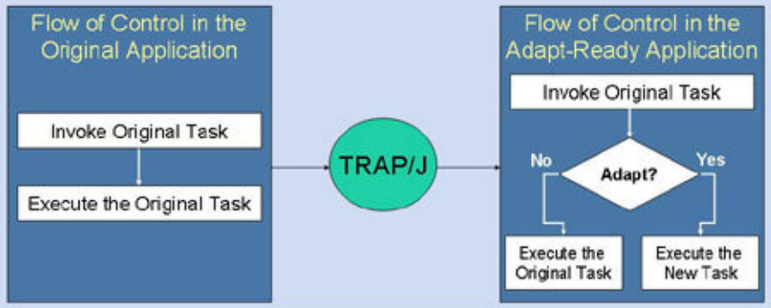

III. Background Information: GRID Superscalar

- GRID superscalar is a new programming paradigm for GRID enabling applications. With GRID superscalar a sequential application, composed of tasks of certain granularity, is automatically converted into a parallel application where the tasks are executed in different servers of a computational GRID.

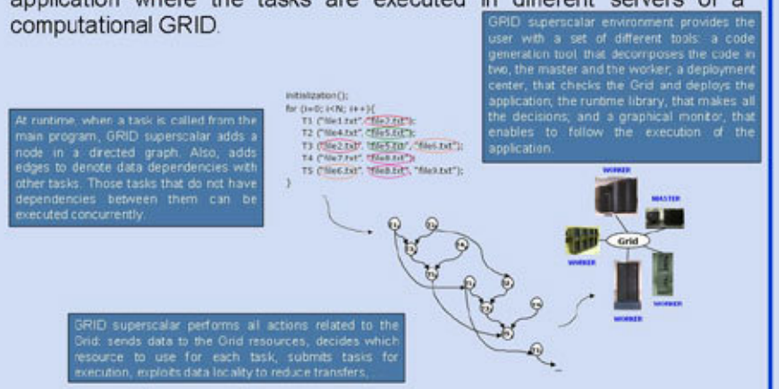

IV. Activity Diagram: Integration Approach with Matrix Multiplication Case Study

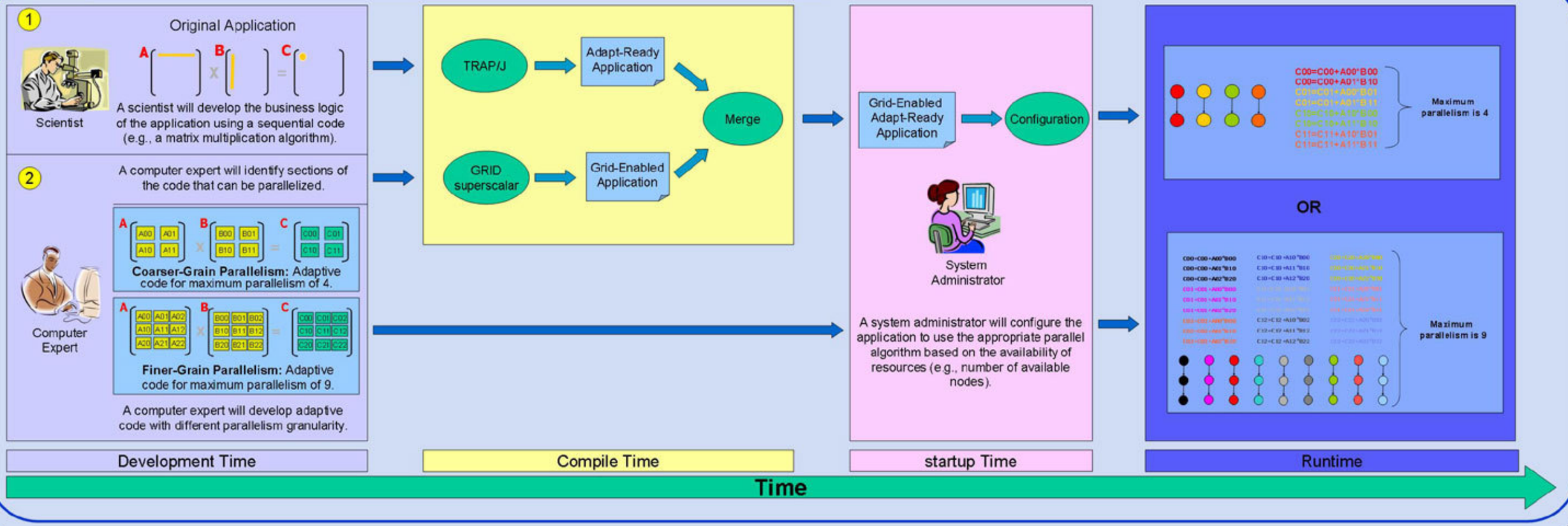

-RESULTS-

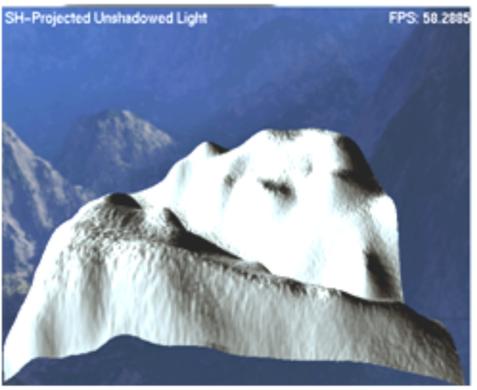

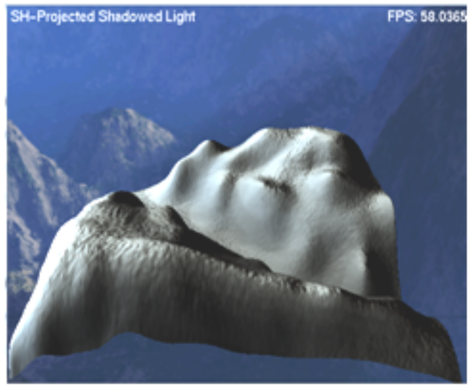

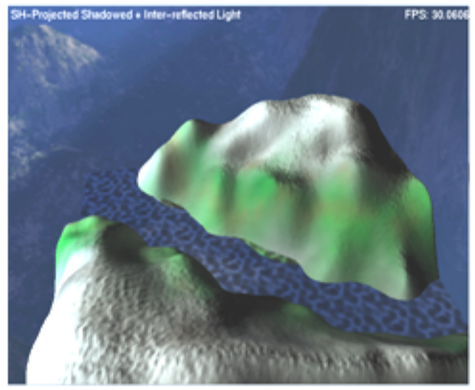


```
****************************************
KEYS:
Q/E : Toggle application modes
W/S/A/D : Move camera (in certain appmodes)
R/F : Up/Down camera (in certain appmodes)
U : Toggle water surface On/Off (in certain appmodes)
Left click + Mouse : Rotate View
****************************************

******LOADING******
Number of SH samples : 300
Preparing spherical function stratified samples...          [Done]
Loading time : 0.000000 seconds

Projecting test light function to SH coefficients...        [Done]
Loading time : 0.000000 seconds

Loading textures...                                         [Done]
Loading time : 0.624000 seconds

SH calculations for unshadowed SH lighting...               [Done]
Loading time : 0.437000 seconds

SH calculations for shadowed SH lighting...                 [Done]
Loading time : 2.294000 seconds

SH calculations for untextured shadowed indirect SH lighting... [Done]
Loading time : 7.519000 seconds

SH calculations for coloured shadowed indirect SH lighting...   [Done]
Loading time : 7.457000 seconds


Total loading time : 18.331 seconds
```

~60fps w/o water plane ~30fps with

-CONCLUSION-

✓**Successful, lightweight and compact implementation of a real-time Global Illumination algorithm with significantly low hardware requirements**

FURTHER WORK :

- **Optimise algorithm**
- **Dynamic objects**
- **True real-time**

Acknowledgements

I would offer my greatest thanks to the following people :
Matthew Bett – Technical Supervisor
Dr. Suheyl Ozveren – Module lecturer
My wife and family

-Algorithm pseudo code-

```
// Precomputation:
Prepare the stratified spherical samples;
Load the bitmaps;
Create 'mesh' object;

// Vertex basic initialization
foreach(vertex in mesh)
{
                initVertex(vertex, X,Y, height, colour, normal, etc...)
                vertexPointers[X][Y] = vertex;
}

// Vertex SH coefficients initialization
foreach(vertex in mesh)
{
                projectVertexConsideringSelfShadowing( vertex );
}

// Inter-reflected light calculation - additional step after shadowing
accumulatedLightSHcoeffs[num_of_vertices];
for(number_of_interreflected_bounces) // usually one is enough
{
                foreach(vertex in mesh)
                {
                                accumulatedLightSHcoeffs[vertex] =
                calcIndirectCoef( vertex );
                }

                foreach(vertex in mesh)
                {
                                vertex.SHcoeffs +=
                accumulatedLightSHcoeffs[vertex];
                }
}

// OpenGL display method called each frame, real-time
display()
{
  Rotate the hardcoded HDR environment light coefficients;

  foreach(vertex in mesh)
  {
    vertex.finalColour = dotProduct(vertex.SHcoeefs, rotatedLightCoeffs);
  }

  Draw the vertices using their finalColour;
}
```

Quantifying the Effect of Pulsatile Fluid Flow on Drug Distribution in the Spinal Canal

Timothy J. Harris Jr., Ying Hsu, Brian Sweetman, H.D.M. Hettiarachchi, Richard Penn MD, and Andreas A. Linninger
Laboratory for Product and Process Design
Department of Bioengineering, University of Illinois at Chicago
BMES National Conference

Drug Distribution in CNS After IT Bolus Infusion

From MRI imaging to computational modeling using first principles fluid mechanics

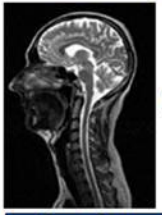

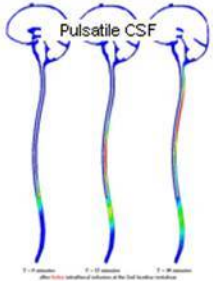

Equations

Continuity equation

$$\nabla \cdot \vec{v} = 0$$

Navier Stokes equation

$$\frac{\partial}{\partial t}(\rho \vec{v}) + \nabla \cdot (\rho \vec{v}\vec{v}) = -\nabla p + \nabla \cdot (\bar{\bar{\tau}}) + \rho \vec{g} + \vec{F}$$

Species Transport equation

$$\frac{\partial C}{\partial t} + \vec{u}(x,t)\nabla C = \nabla D \nabla C + R$$

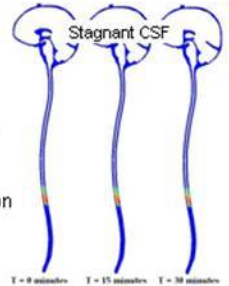

Motivation

Intrathecal (IT) Delivery

- Bypasses blood brain barrier
- Delivers macromolecules to the brain tissue via the interconnected cerebrospinal fluid space
- Applications include proteins, nanoparticles and gene therapy using viral vectors

Experimental & Computational Validation

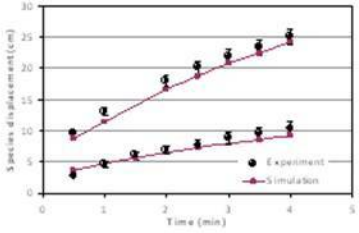

Computational Modeling of Spinal Canal with Cord

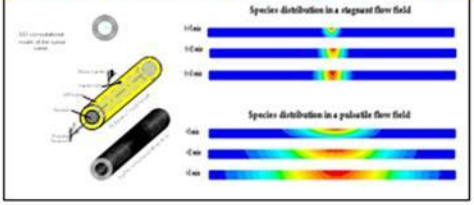

Future Work

Build three dimensional experimental and computational models to predict the outcome of IT treatment in the entire human CNS.

Experimental Set-Up

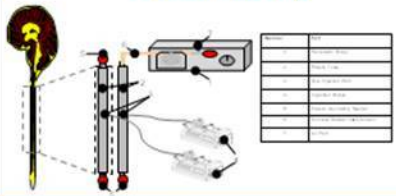

Nuclear Medicine Results

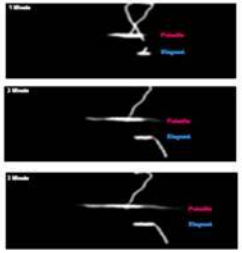

Distribution of Tc vs. Time in a Pulsatile and Stagnant System

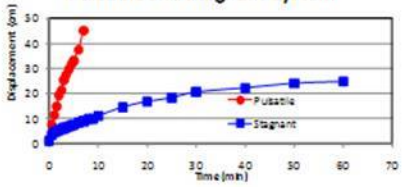

Technetium-99m displacement with time for pulsatile and stagnant flow experiments. At seven minutes, pulsatile flow shows over 500% increase in displacement compared to stagnant flow experiments.

An Optimization Algorithm for the Identification of Biochemical Network Models

www.math.vt.edu

M. Paola Vera-Licona, Luis David Garcia, John McGee, Miguel Colon-Velez and Reinhard Laubenbacher
mveralic@.math.vt.edu

www.vbi.vt.edu

INTRODUCTION

An important problem in computational biology is the modeling of several types of networks, ranging from gene regulatory networks and metabolic networks to neural response networks.

In [LS], Laubenbacher and Stigler presented an algorithm that takes as input time series of system measurements, including certain perturbation time series, and provides as output a discrete dynamical system over a finite field.

Since functions over finite fields can always be represented by polynomial functions, one can use tools from computational algebra for this purpose. The key step in the algorithm is an interpolation step, which leads to a model that fits the given data set exactly. Due to the fact that biological data sets tend to contain noise, the algorithm leads to over-fitting.

Here we present a genetic algorithm, that optimizes the model produced by the Laubenbacher-Stigler algorithm between model complexity and data fit. This algorithm (implemented in C++), uses tools from computational algebra in order to provide a computationally simple description of the mutation rules.

DISCRETE POLYNOMIAL MODELS

A **discrete polynomial model** is a vector function

$$f = (f_1,\ldots,f_n) : \mathbb{F}^n \rightarrow \mathbb{F}^n$$

where $\mathbb{F}$ is a finite field and $f_i : \mathbb{F}^n \rightarrow \mathbb{F}$, are local update polynomials for each node $i = 1,\ldots,n$.

The phase space of a polynomial model, is given by the directed graph, where:

vertices := states of system
Edge from v_j to v_k iff $f(v_j)=v_k$

Therefore a time series is represented as a path in this graph.

Example of a model and phase space graph

$f = (f_1, f_2) : \{1,0,\}^2 \rightarrow \{1,0\}^2$
$f_1 = x_1 + x_2$
$f_2 = x_1 + 1$

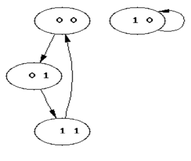

GENETIC ALGORITHM

1. Elements of the Genetic Algorithm

Genome: A finite dynamical system model as a set of d polynomials over $\mathbb{F}_2$ (finite field of 2 elements)

Fitness function: Hamming distance between time series generated by the model and the input time series along with a measure of model complexity

Mutated Initial States: Improve robustness of estimated model

Mutation: Addition or removal of one variable from one monomial

Crossover: Creation of a Polynomial as mixture of subsets of the monomials from two parent models.

2. Input Data

Time Series: A set of discrete time series over $\mathbb{F}_2$, with different initial states

Knockout Data: Perturbed data from the knockout of some or all of the entities in the network

Candidate Model: Obtained by applying L-S algorithm to the available data.

3. Effectiveness of Fitness Score

We used empirical measurements to verify that if an estimated model is close to the true model, then the time series produced by the estimated model will have a small Hamming distance from that produced by the true model from the same initial state.

Figure 1 plots h for the values of d up to 30, where d is the number of mutations between two models, and h is the average Hamming distance between time series produced by the two models.

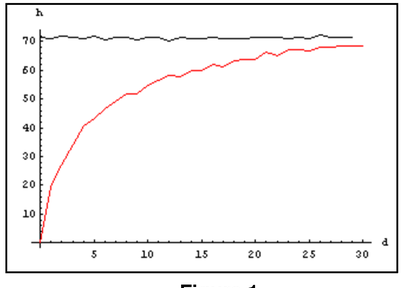

Figure 1

GENETIC ALGORITHM

3. Parameters of Genetic Algorithm

In order to control the evolutionary search for a satisfactory solution model, our genetic algorithm uses 12 parameters (e.g. population size, mutation rate, crossover rate, etc).

The tuning of this set of parameters is one main feature in the early stage of this project.

4. Computational Algebra Tools

We formulated an upper bound for the number of variables in every monomial, given the input time series samples. This formulation is based on the maximum support of a monomial member of any Gröbner basis of the ideal that vanishes on a time series t, which greatly restricts the genetic algorithm search space, improving the efficiency of the optimization.

Testing and Tuning

We employed an 8-variable model to generate time series and perturbed data, as input into the Laubenbacher-Stigler method and/or directly as input into the genetic algorithm.

The performance of the G.A. is significantly improved when the model from L-S was used as input in the G.A.

$f_1 = x_1 + x_2$
$f_2 = x_2 + x_3x_5$
$f_3 = x_3 + x_4x_6$
$f_4 = x_4 + x_8$
$f_5 = x_5 + x_3$
$f_6 = x_6$
$f_7 = x_7$
$f_8 = x_8 + x_1$

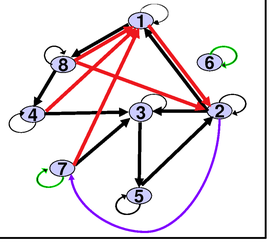

Figure 2. On the left, model used. On the right, Topology of the model used. In black is the intersection of the graphs produced by the original model, L-S model and that obtained from the genetic algorithm. In red are the extra links that the last two share and finally, the purple link is the extra link that L-S model has and that the genetic algorithm was able to delete.

APPLICATIONS

Network of the Segment Polarity Genes in the Fruit Fly *D. Melanogaster*

This network consists of the genes whose function is to define the segment boundaries and polarity in the *D. melanogaster* embryo. Each one of the four cells in the network consists of 5 genes and the products encoded by them, as well as two protein compounds and 6 more elements from neighbor cells.

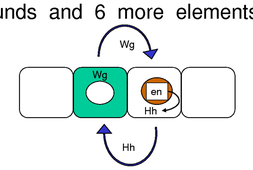

We perform a series of experiments on the 21-variable model obtained in [LS] , adjusting our method by applying the genetic algorithm twice.

Label of Parameter Set	Corrected links	Loops deleted
1.2.	3	1
2.2.	6	2
3.3.	3	1
5.2.	2	0

Table 1. Considering [AO] model (21 nodes and 44 links), we compare our results with [LS]. The second column refers to the number of excessive links in [LS] topology that the G.A. corrected and the second column represents the number of loops that the G.A. deleted.

FINAL COMMENTS

1. Initial results indicate that our Genetic Algorithm approach to either discovery or refinement of a dynamical system model can be an effective element of a robust system for genetic network identification.
2. An extension of this algorithm for more general finite fields is being performed as part of a second phase of this project.

REFERENCES

[LS] R. Laubenbacher and B. Stigler, A Computational Algebra Approach to the Reverse Engineering of Gene Regulatory Networks

[BO] E. Babson, S. Onn. The Hilbert Zonotope and a Polynomial Time Algorithm for Universal Grobner Bases. 2003

[HC] Hochmuth Gregor, On the Genetic Evolution of a Perfect Tic-Tac-Toe Strategy

[AO] R. Albert and H. Othmer. The Topology of the Regulatory Interactions Predicts the Expression Pattern of the Segment Polarity Genes in *Drosophila melanogaster.*

Logistic Regression for Single-trial EEG Classification

Ryota Tomioka[13], Kazuyuki Aihara[1], & Klaus-Robert Müller[23]

[1]The University of Tokyo, [2]Technical University of Berlin, & [3]Fraunhofer FIRST.IDA

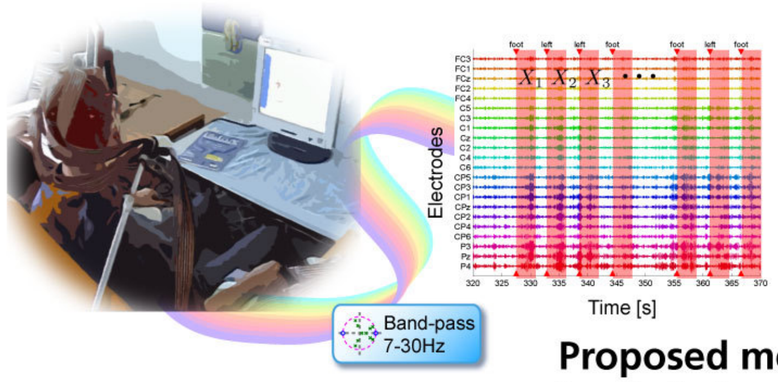

Epoched EEG: $X_1\ X_2\ X_3\ \cdots$ ($d \times T$)

Sensor covariance of the epoched EEG: $X_i X_i^\top$ ($d \times d$) (i=1,...,n)

d: #channels
T: #sampled time-points
n: #examples

Optimality?
Number of components?
Selecting components?

Conventional approach: Classifying with CSP

Classwise covariance matrix

$$\Sigma^{(c)} = \frac{1}{|\mathcal{I}^c|} \sum_{i \in \mathcal{I}^c} X_i X_i^\top \qquad (c \in \{+,-\}),$$

Simultaneous diagonalization, [Fukunaga 1972, Koles 1991]
i.e., a Generalized Eigenvalue Problem (GEP).

$$\Sigma^{(+)} \boldsymbol{w} = \lambda \Sigma^{(-)} \boldsymbol{w}$$

LDA on the log-power features

$$f_{\mathrm{CSP}}\left(X; \{\boldsymbol{w}_j\}_{j=1}^J, \{c_j\}_{j=0}^J\right) = \sum_{j=1}^J c_j \log \boldsymbol{w}_j^\top X X^\top \boldsymbol{w}_j + c_0$$

Proposed method: Logistic Regression (LR) classifier

We model the symmetric logit transform of the conditional probability

$$\log \frac{P(y=+1|X)}{P(y=-1|X)} = f(X;\boldsymbol{\theta})$$

Full-rank symmetric matrix parameterization

Linearly classify w.r.t. the sensor-covariance coefficients

$$\min_{W \in \mathrm{Sym}(d), b \in \mathbb{R}} \frac{1}{n} \sum_{i=1}^n \log\left(1 + e^{-y_i f(X_i;\boldsymbol{\theta})}\right) + \frac{C}{2} \mathrm{tr} \Sigma W \Sigma W$$

$$f(X;\boldsymbol{\theta}) = \mathrm{tr}\left[W X X^\top\right] + b$$

$$\boldsymbol{\theta} := (W, b) \in \mathrm{Sym}(d) \times \mathbb{R}$$

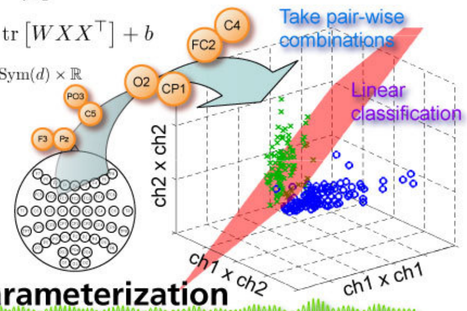

How is it related to a generative model?

Zero-mean Gaussian with no temporal correlation

$$P(X|c) \propto \prod_{t=1}^T \exp\left\{-\frac{1}{2} \boldsymbol{x}_t^\top \Sigma^{(c)^{-1}} \boldsymbol{x}_t\right\}$$
$$= \exp\left\{-\frac{1}{2} \mathrm{tr}\left[\Sigma^{(c)^{-1}} X X^\top\right]\right\} \qquad (c \in \{+,-\})$$

leads to the discriminative model we use!

$$\log \frac{P(y=+1|X)}{P(y=-1|X)} = \frac{1}{2} \mathrm{tr}\left[\left(-\Sigma^{(+)^{-1}} + \Sigma^{(-)^{-1}}\right) X X^\top\right] + \mathrm{const.}$$

Rank=2 parameterization

The classifier is approximated with the difference of two rank=1 matrices

$$\min_{\boldsymbol{w}_1, \boldsymbol{w}_2 \in \mathbb{R}^d, b \in \mathbb{R}} \frac{1}{n} \sum_{i=1}^n \log\left(1 + e^{-y_i \bar{f}(X_i;\bar{\boldsymbol{\theta}})}\right)$$
$$+ \frac{C}{2}\left(\boldsymbol{w}_1^\top \Sigma \boldsymbol{w}_1 + \boldsymbol{w}_2^\top \Sigma \boldsymbol{w}_2\right) \qquad (1)$$

The pooled covariance matrix is introduced to ensure invariance to linear transformations.
$\Sigma = \frac{1}{n} \sum_{i=1}^n X_i X_i^\top$

$$\bar{f}(X;\bar{\boldsymbol{\theta}}) := \frac{1}{2} \mathrm{tr}\left[\left(-\boldsymbol{w}_1 \boldsymbol{w}_1^\top + \boldsymbol{w}_2 \boldsymbol{w}_2^\top\right) X X^\top\right] + b,$$

$$\bar{\boldsymbol{\theta}} := (\boldsymbol{w}_1, \boldsymbol{w}_2, b) \in \mathbb{R}^d \times \mathbb{R}^d \times \mathbb{R}$$

Classification performance

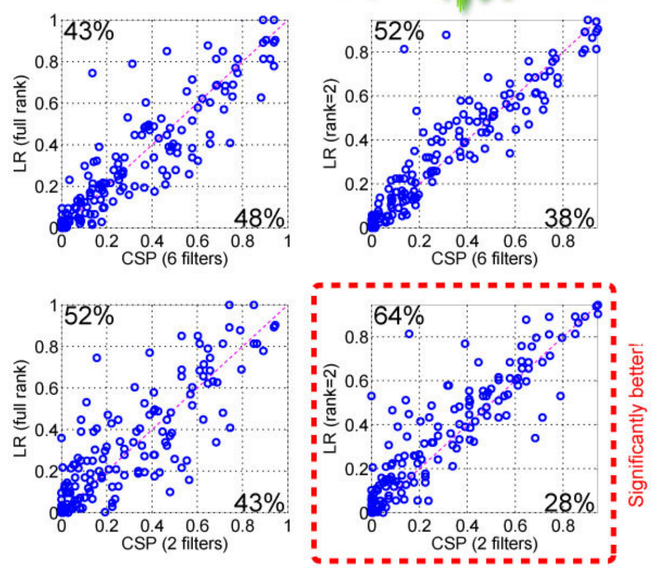

Experimental setups

Paradigm: motor imagination: "left hand", "right hand" or "foot".
Instruction: visual cue "L", "R", or "F" on the screen.
Feedback: no feedback (calibration measurements).
Sampling: recorded at 1000Hz. down-sampled to 100Hz.
Electrodes: 32, 64, or 128 channels. #subjects=29. #datasets=162.
Preprocessing: band-pass filtered at 7-30Hz.
Training and testing: chronological split, i.e., all methods are trained on the first half and tested on the second half.
Performance measure: bits per decision:

$$1 - \left(p_{\mathrm{err}} \log_2 \frac{1}{p_{\mathrm{err}}} + (1 - p_{\mathrm{err}}) \log_2 \frac{1}{1 - p_{\mathrm{err}}}\right)$$

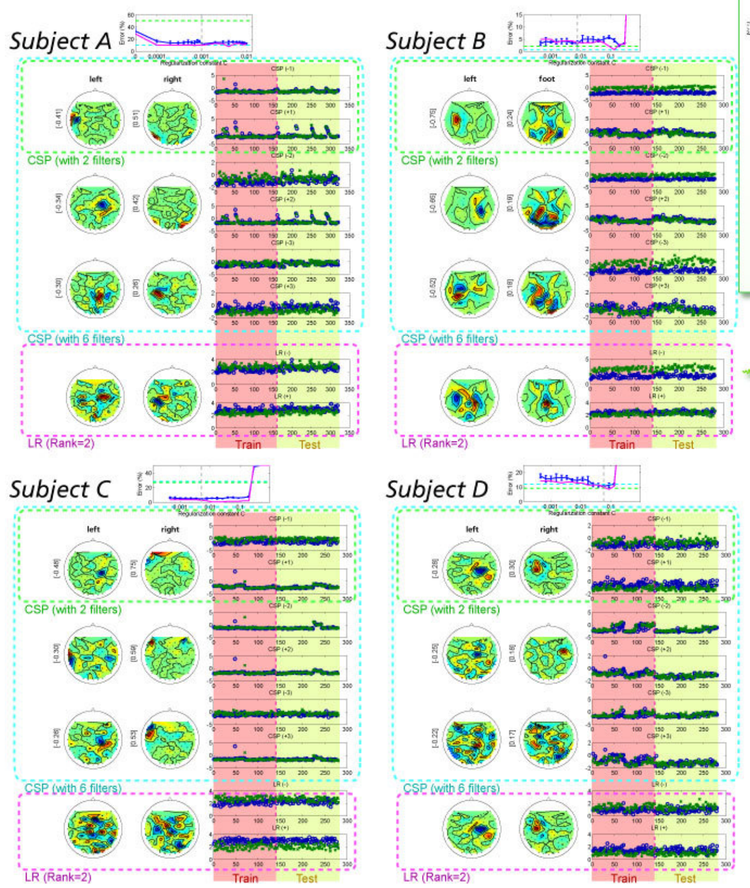

Connection between the rank=2 parametrization and CSP

Differentiating (1) w.r.t. $\boldsymbol{w}_j$ at the optimum $\bar{\boldsymbol{\theta}}^*$

$$\pm \frac{1}{n} \sum_{i=1}^n \frac{e^{-z_i}}{1 + e^{-z_i}} y_i X_i X_i^\top \boldsymbol{w}_j^* + C \Sigma \boldsymbol{w}_j^* = 0 \qquad (j = 1, 2)$$

where $z_i := y_i \bar{f}(X_i; \bar{\boldsymbol{\theta}}^*)$.

Recalling that $\Sigma = \frac{1}{n} \sum_{i=1}^n X_i X_i^\top$, we obtain a pair of GEPs (find eigenvectors with unit eigenvalues):

$$\Sigma^{(-)}(\bar{\boldsymbol{\theta}}^*, 0) \boldsymbol{w}_1^* = \Sigma^{(+)}(\bar{\boldsymbol{\theta}}^*, C) \boldsymbol{w}_1^*$$
$$\Sigma^{(+)}(\bar{\boldsymbol{\theta}}^*, 0) \boldsymbol{w}_2^* = \Sigma^{(-)}(\bar{\boldsymbol{\theta}}^*, C) \boldsymbol{w}_2^*$$

where we define the uncertainty weighted covariance matrix as:

$$\Sigma^{(\pm)}(\bar{\boldsymbol{\theta}}^*, C) = \sum_{i \in \mathcal{I}_\pm} \frac{e^{-z_i}}{1 + e^{-z_i}} X_i X_i^\top + C \sum_{i=1}^n X_i X_i^\top$$

$= 1 - P(y = y_i | X = X_i)$ — Regularization

Small weight	Classifier is certain about the decision.
Large weight	Classifier is uncertain about the decision.

because,

$$z_i = y_i \bar{f}(X_i; \bar{\boldsymbol{\theta}}^*) = \log \frac{P(y = y_i | X = X_i)}{P(y \neq y_i | X = X_i)}$$

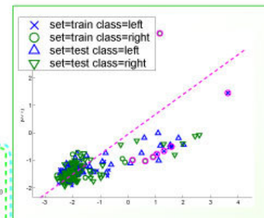

Low dimensional feature space using CSP for Subject A. "outliers" are marked magenda.

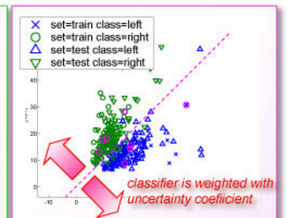

Low dimensional feature space using logistic regression (rank=2) for Subject A. "outliers" are marked magenda.

Conclusion

Logistic regression for the classification of single trial motor-imagery EEG

- Classifies linearly in the space of variance and covariances
- a discriminative model, i.e., the marginal density P(X) is left unestimated.
- the classifier output has a probabilistic interpretation.
- the classification problem is formulated under a single optimization problem.

(a) *Full-rank symmetric matrix parametrization*
- convex optimization.
- connection to a generative model.

(b) *Rank=2 approximation*
- improved physiological interpretability.
- connection to CSP [Koles, 1991].
- comparable or favorable performance to CSP with 6 filters or 2 filters, respectively.

Analysis of Biomedical Images using Adaptive Computer Vision

William M. Beaver and Yoav Freund
Department of Computer Science and Engineering
{wbeaver, yfreund}@cs.ucsd.edu

Problem

The rapid advancement of biomedical imaging techniques such as fluorescence microscopy, non-linear optics, MRI and ultra-sound make it now possible to observe the time evolution of mechanical and biochemical processes in cells and in the human body at a resolution unimaginable a decade ago. This ability to measure opens up an incredible range of new possibilities for research in biology and in medicine. However, a major challenge along the way is the formidable amount of manual work required to extract meaningful quantitative results from the enormous amounts of collected image data.

Our Approach

We use an adaptive process of computer vision and machine learning that views algorithmic selection and tuning as search problems. We embrace the domain experts and expect them to direct the search and learning process by "teaching" the algorithm where to look for the interesting and significant features.

Our process requires domain expert input to identify salient features, and we allow them to use the data representation they find most effective for labeling. We have integrated our XML–annotation into the NIH's open source program ImageJ and into Matlab. Learning platform varies on solution.

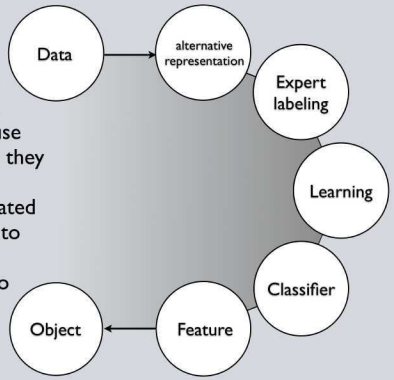

Real-time and high-throughput analysis are our goals, and to that end we explore the use of graphics hardware (GPUs) to perform search.

Future Directions include

- an adaptive platform that selects appropriate configuration and search space options to allow domain expert to focus on problem at hand rather than on image processing intricacies.
- automatic object/element tracking
- real-time analysis
  - static: movies, image stacks, etc.
  - dynamic: on microscope, camera
- homogenous environment; ideally integrated into devices for real-time, "anywhere" processing.

Collaboration with Sheetz Lab, Columbia University

Grégory Giannone, Benjamin Dubin-Thaler, Hans-Günther Döbereiner, and Michael P. Sheetz

Objective: Show how lamellipodial actin acts as mechanical contractile signal for cell motility.

Contribution: Provide automated analysis of DIC and α-actinin TIRF microscopy based on interactively defined features of interest (FOI).

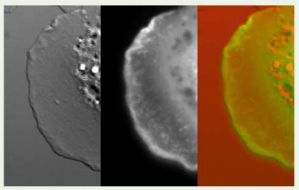

Frame from a movie of mouse embryonic fibroblast (MEF) spreading on fibronectin (FN). This is an example of both DIC and α-actinin TIRF microscopy plus a visualization combining both.

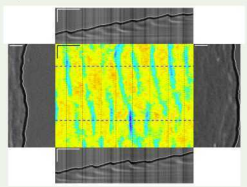

Velocity map of leading cell edge. Additional FOIs (wave summits) are highlighted in Kymographs. These are normally qualitatively, rather than quantitatively, analyzed.

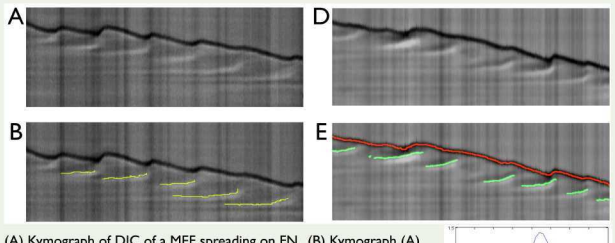

(A) Kymograph of DIC of a MEF spreading on FN. (B) Kymograph (A) with FOI annotated in ImageJ by human using our annotation tool. In this example the FOI is the summit of the backward moving waves. (C) Signal response filter learned to match FOIs as defined by (B). (D) New kymograph of DIC taken from kymograph adjacent to (A). (D) FOIs found automatically in (D). Green indicates wave summit of backward moving waves found using signal response filter (C). Red is cell edge.

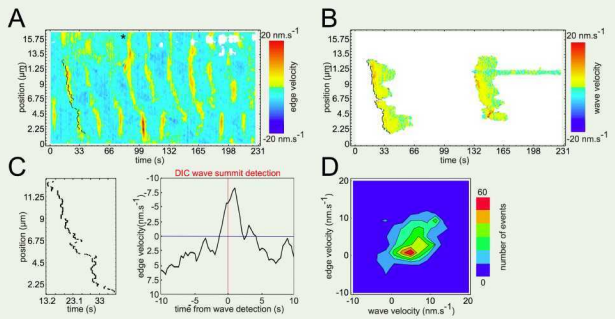

(A) Edge velocity plotted as a function of time and position along the cell edge of a spreading MEF. (B) Wave velocity plotted as a function of time and position along the cell edge, giving a velocity map of two waves generated during retraction from the DIC time-lapse in (A). (C) The initial detection of the DIC wave summit (C, left) corresponded to the peak of the retraction (A, overlaid line). Close analysis of the correspondence by plotting velocity versus time from DIC wave initiation (red line) (C, right). (D) The speed of DIC wave retractions correlated to the speed of the edge retraction.

Collaboration with McGinnis Lab, UCSD

Gary Tedeschi, Dave Kosman, and William McGinnis

Objective: Quantify spatial and temporal correlations between gene expression during *Drosophila* development.

Contribution: Provide image segmentation and 3D spatial reconstruction of gene transcripts from multichannel confocal microscopy.

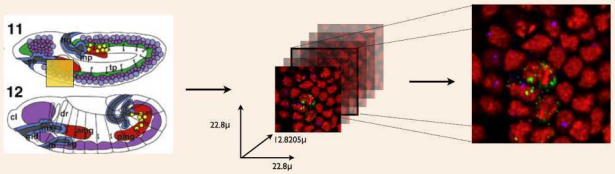

(left) Region of interest in the second thoracic segment of a stage 11 *Drosophila* embryo.[1] (middle) Image stacks representing ~20 ectodermal cells .There are 35 slices in each image stack at resolution of 300x300 pixels.
(right) The cells include limb field cells as indicated by the marker for the Distalless transcript (*Dll*; here blue); DNA is marked with *dapi* stain (here red) and *wingless (wg)* transcript (here green).

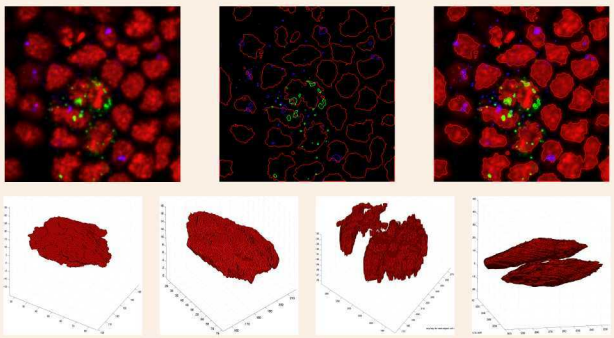

(TOP) (left) Representative confocal image containing multiple channels of gene expression: DNA (red), *Dll* (blue) and *wg* transcript (green). (middle) Image segmentation by channel via threshold. (right) Confocal image + segmentation. While segmentation appears qualitatively accurate, analysis is complicated by fact that not all detections are biologically significant. For example, most of the *Dll* detections in this example are cytoplasmic and not meaningful.
(BOTTOM) Volume representations of 3D segmentations. Two leftmost examples each reflect accurate segmentation of nucleus. Two rightmost volumes reflect common problem with many segmentation results; namely merging of distinct objects.

For each biologically meaningful segmentation (as determined by a domain expert) we use PCA to extract various moments.

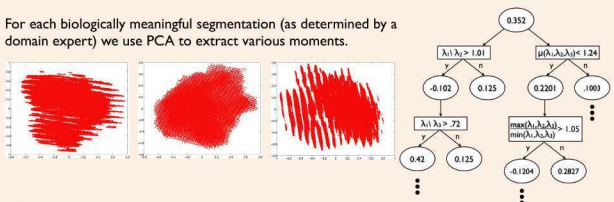

With these features we use Adaboost to generate a classifier. Adaboost outputs an alternating decision tree (right) predictor which we use to classify future objects given a segmented image stack.

[1] Bate, Martinez Arias, "The development of *Drosophila melanogaster*." Cold Spring Harbor Laboratory Press, 1993

PIGS IN SPACE: EFFECT OF ZERO GRAVITY AND AD LIBITUM FEEDING ON WEIGHT GAIN IN CAVIA PORCELLUS

Colin B. Purrington
6673 College Avenue, Swarthmore, PA 19081 USA

ABSTRACT:

One ignored benefit of space travel is a potential elimination of obesity, a chronic problem for a growing majority in many parts of the world. In theory, when an individual is in a condition of zero gravity, weight is eliminated. Indeed, in space one could conceivably follow ad libitum feeding and never even gain an gram, and the only side effect would be the need to upgrade one's stretchy pants("exercise pants"). But because many diet schemes start as very good theories only to be found to be rather harmful, we tested our predictions with a long-term experiment in a colony of Guinea pigs (Cavia porcellus) maintained on the International Space Station. Individuals were housed separately and given unlimited amounts of high-calorie food pellets. Fresh fruits and vegetables were not available in space so were not offered. Every 30 days, each Guinea pig was weighed. After 5 years, we found that individuals, on average, weighed nothing. In addition to weighing nothing, no weight appeared to be gained over the duration of the protocol. If space continues to be gravity-free, and we believe that assumption is sound, we believe that sending the overweight — and those at risk for overweight — to space would be a lasting cure.

INTRODUCTION:

The current obesity epidemic started in the early 1960s with the invention and proliferation of elastane and related stretchy fibers, which released wearers from the rigid constraints of clothes and permitted monthly weight gain without the need to buy new outfits. Indeed, exercise today for hundreds of million people involve only the act of wearing stretchy pants in public, presumably because the constrictive pressure forces fat molecules to adopt a more compact tertiary structure (Xavier 1965).

Luckily, at the same time that fabrics became stretchy, the race to the moon between the United States and Russia yielded a useful fact: gravity in outer space is minimal to nonexistent. When gravity is zero, objects cease to have weight. Indeed, early astronauts and cosmonauts had to secure themselves to their ships with seat belts and sticky boots. The potential application to weight loss was noted immediately, but at the time travel to space was prohibitively expensive and thus the issue was not seriously pursued. Now, however, multiple companies are developing cheap extra-orbital travel options for normal consumers, and potential travelers are also creating news ways to pay for products and services that they cannot actually afford. Together, these factors open the possibility that moving to space could cure overweight syndrome quickly and permanently for a large number of humans.

We studied this potential by following weight gain in Guinea pigs, known on Earth as fond of ad libitum feeding. Guinea pigs were long envisioned to be the "Guinea pigs" of space research, too, so they seemed like the obvious choice. Studies on humans are of course desirable, but we feel this current study will be critical in acquiring the attention of granting agencies.

MATERIALS AND METHODS:

One hundred male and one hundred female Guinea pigs (Cavia porcellus) were transported to the International Space Laboratory in 2010. Each pig was housed separately and deprived of exercise wheels and fresh fruits and vegetables for 48 months. Each month, pigs were individually weighed by duct-taping them to an electronic balance sensitive to 0.0001 grams. Back on Earth, an identical cohort was similarly maintained and weighed. Data was analyzed by statistics.

RESULTS:

Mean weight of pigs in space was 0.0000 +/- 0.0002 g. Some individuals weighed less than zero, some more, but these variations were due to reaction to the duct tape, we believe, which caused them to be alarmed push briefly against the force plate in the balance. Individuals on the Earth, the control cohort, gained about 240 g/month ($p = 0.0002$). Males and females gained a similar amount of weight on Earth (no main of effect of sex), and size at any point during the study was related to starting size (which was used as a covariate in the ANCOVA). Both Earth and space pigs developed substantial dewlaps (double chins) and were lethargic at the conclusion of the study.

CONCLUSIONS:

Our view that weight and weight gain would be zero in space was confirmed. Although we have not replicated this experiment on larger animals or primates, we are confident that our result would be mirrored in other model organisms. We are currently in the process of obtaining necessary human trial permissions, and should have our planned experiment initiated within 80 years, pending expedited review by local and Federal IRBs.

ACKNOWLEDGEMENTS:

I am grateful for generous support from the National Research Foundation, Black Hole Diet Plans, and the High Fructose Sugar Association. Transport flights were funded by SPACE-EXES, the consortium of wives divorced from insanely wealthy space-flight startups. I am also grateful for comments on early drafts by Mañana Athletic Club, Corpus Christi, USA. Finally, sincere thanks to the Cuy Foundation for generously donating animal care after the conclusion of the study.

LITERATURE CITED:

NASA. 1982. Project STS-XX: Guinea Pigs. Leaked internal memo.

Sekulić, S.R., D. D. Lukač, and N. M. Naumović. 2005. The Fetus Cannot Exercise Like An Astronaut: Gravity Loading Is Necessary For The Physiological Development During Second Half Of Pregnancy. Medical Hypotheses. 64:221-228

Xavier, M. 1965. Elastane Purchases Accelerate Weight Gain In Case-control Study. Journal of Obesity. 2:23-40.

Pinning Effects in Two-Band Superconductors

Chad Sockwell, Max Gunzburger, Janet Peterson

Scientific Computing, Florida State University, Email: kcs12j@my.fsu.edu

Objectives

- Numerically simulate the vortex dynamics in the superconducting material MgB_2.
- Devise a way to raise the maximum amount of current carried in the superconductor.
- Simulate how impurities raise the maximal current in MgB_2.

Introduction

Most are familiar with the waste heat produced by resistance in an electrical wire. This wasted energy can be avoided by using resistance free superconductors. However superconductors posses critical (maxiumum) values for their temperature, magnetic field, and current, only below which they operate as resistance free. Introducing impurities can raise the critical current by preventing flux flow. Practical superconducting devices could revolutionize technology but numerical simulations are needed to give insight.

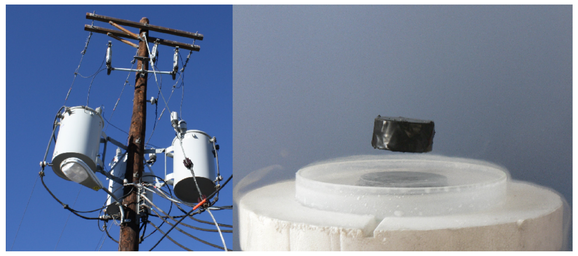

MgB_2

- Magnesium Diboride (MgB_2) is a two band superconductor that can carry resistance free current under a temperature of 39K (-389.47 ° F).
- The bands act as pathways for electrons, each possessing their own properties seen in Table 1 .
- The bands interact to give composite direction and temperature dependent magnetic properties.

λ_1=47.8 nm	λ_2= 36.6 nm	ξ_1=13 nm	ξ_2=51 nm
κ_1=3.61	κ_2=0.658	$\nu = 2.757$	$\eta = -0.1701$

Table 1: The material parameters for MgB_2.

Flux Flow

- In the presence of a external magnetic field, normal materials are completely penetrated by the field. However superconductors such as MgB_2 are only penetrated by small magnetic flux vortices.
- The flux vortices interact with the applied current, **J** to produce a Lorentz force, **F**, perpendicular to **J**.
- The movement of the vortices, known as flux flow, induces an electric field, **E**, parallel to the applied current, creating an effective resistance.
- Figure 3 shows how the force moves the vortices (red) as time increases.

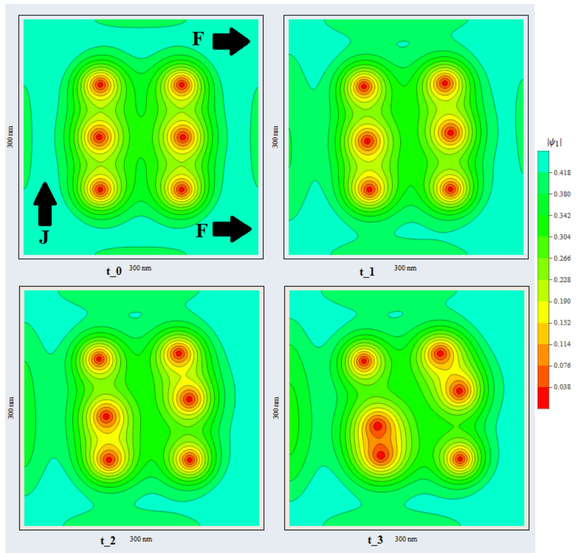

Figure 1: The vortices can be seen where ψ_1 is at is smallest (red). They are pushed to the right by the Lorentz force. At later times (t_3) the vortices rearrange themselves.

Mathematical Model

The Modified 2B-TDGL model describes superconductivity and contains ψ_1 and ψ_2, the density functions for the current carriers, the magnetic vector potential, **A**, and takes the parameters from Table 1 as input. The vortices can be seen where ψ_1 is at its smallest. Numerical simulations of vortex dynamics from the model are seen in Figures 1, 4

Methods

The finite element, Euler, and Newton methods were used together to solve the model equations. Supercomputers were used at F.S.U.'s R.C.C. for calculations.

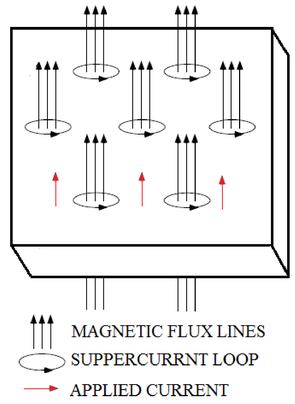

Figure 2: The set up for the numerical simulations. The magnetic field penetrates the sample as flux vortices and an applied current is transported across the sample.

Results

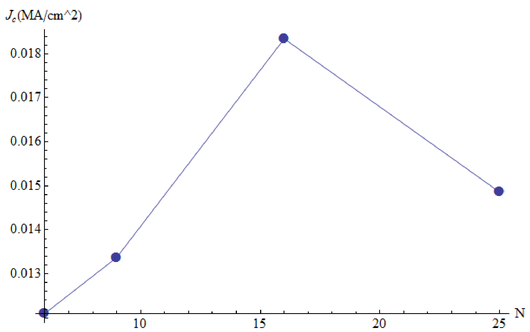

Figure 3: The critical current for different numbers of impurity sites. This under a temperature of 30 K and magnetic field of 0.106 Tesla.

Impurities were successfully modeled in the material. The pinning effects are shown in Figure 4. The impurity sites are outlined by the open black circles. A raise in the critical current J_c was found by increasing the normals N (Figure 3). However too many impurities degraded the superconducting material and lower J_c, as seen where N=25.

Conclusion

MgB_2 was successfully modeled using the simulation. Figure 5 shows directional dependence on the critical magnetic fields, comparable to experiments. An algorithm to model impurities in the sample was successful in raising the critical current.

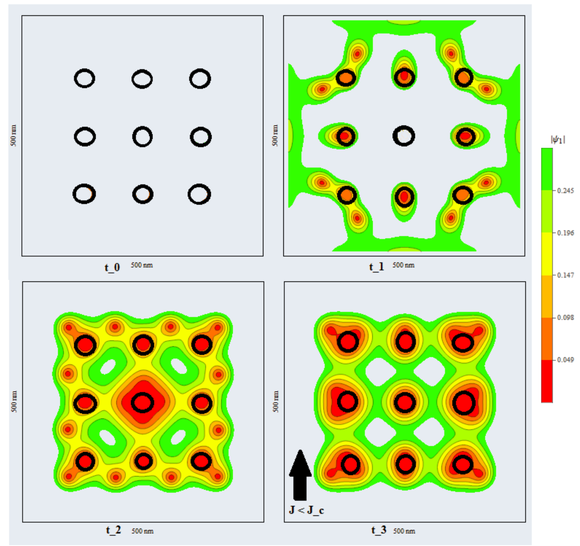

Figure 4: From top left to bottom right, vortices (red) are generated from a magnetic field. They become pinned to the normal site (black circles). When a current **J** is applied, the vortices remained pinned, unlike Figure 2.

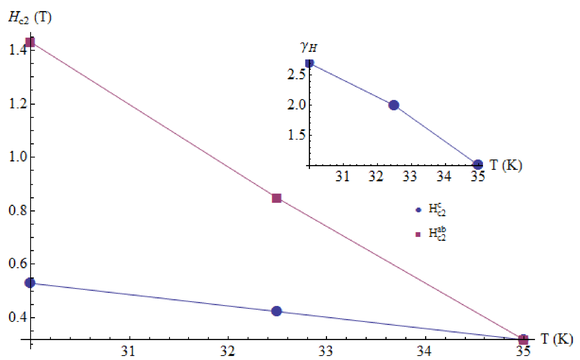

Figure 5: Magnetic properties comparable to experiment, $\gamma_H = H_{c2}^{ab}/H_{c2}^c$.

Acknowledgements: I would like to acknowledge and graciously thank The Center for Undergraduate Research and Academic Engagement at F.S.U. and their private donors for the M.R.C.E. award that supported this research.

To reduce the default rate at Fast Track asthma Clinic (FTC)

Lathy Prabhakaran, Jane C, Abisheganadan J, Liew N L, Fatimah S, Lim G H, Tan W L.
Nursing Service, Respiratory Department, Emergency Department,
Tan Tock Seng Hospital Singapore.

Mission Statement

"To reduce the default rate of referral appointments from ED to the Fast Track asthma Clinic (FTC)* from the current 50% to less then 10% in 6 months"

*FTC –to see new asthma cases referred from ED within 2 weeks

Team Members

Name	Designation	Department
Lathy Prabhakaran (Team Leader)	Senior Nurse Clinician (Asthma Nurse)	Nursing Service
Dr.John Abisheganadan (Facilitator)	Senior Consultant	Respiratory Medicine
Jane Chee	Nursing Clinician (Asthma Nurse)	Nursing Service
Liew Nyuk Lian (Christine)	Patient service assistant	Clinic 2B
Dr. Lim Ghee Hian	Consultant	Emergency
Fatimah Sattar	Patient service assistant	Emergency
Tan Wei Lee	Nursing officer	Emergency

Background

- Fast track asthma clinic was initiated in 2004 for patients seen at ED with poor asthma control to be fast track (expedited) to this clinic to be reviewed by the doctor.
- AT FTC patients are reviewed within two weeks instead of waiting for appointment at respiratory specialist clinic.
- The current waiting time at respiratory specialist clinic is seven weeks.
- Aim is to stabilize and optimize asthma control quickly.

Evidence of a Problem Worth Solving

- Despite the well-intended intervention of developing the fast track asthma clinic, the default rates as been high.

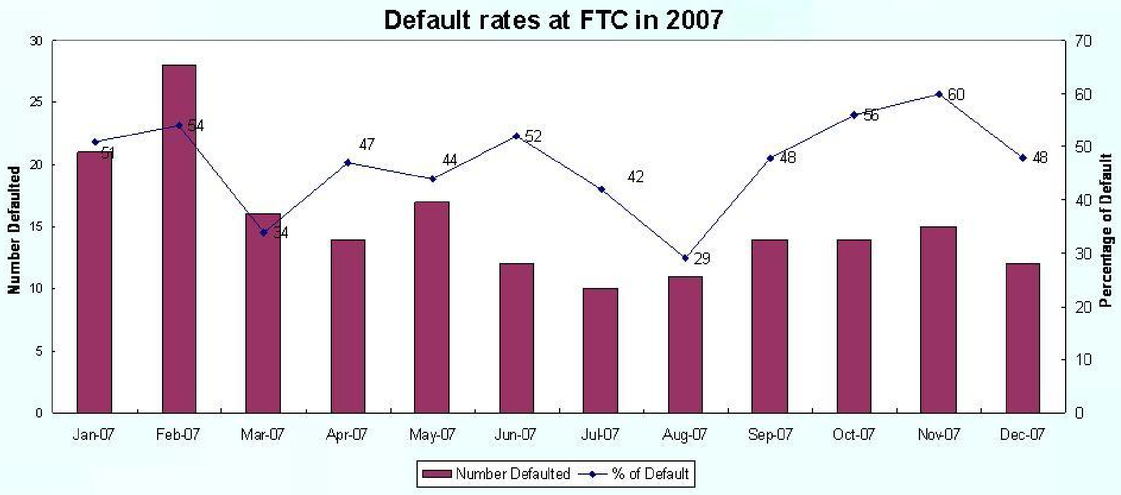

Data source from clinic 2B statistic

Mean Default 46% for year 2007

Flow Chart of Process

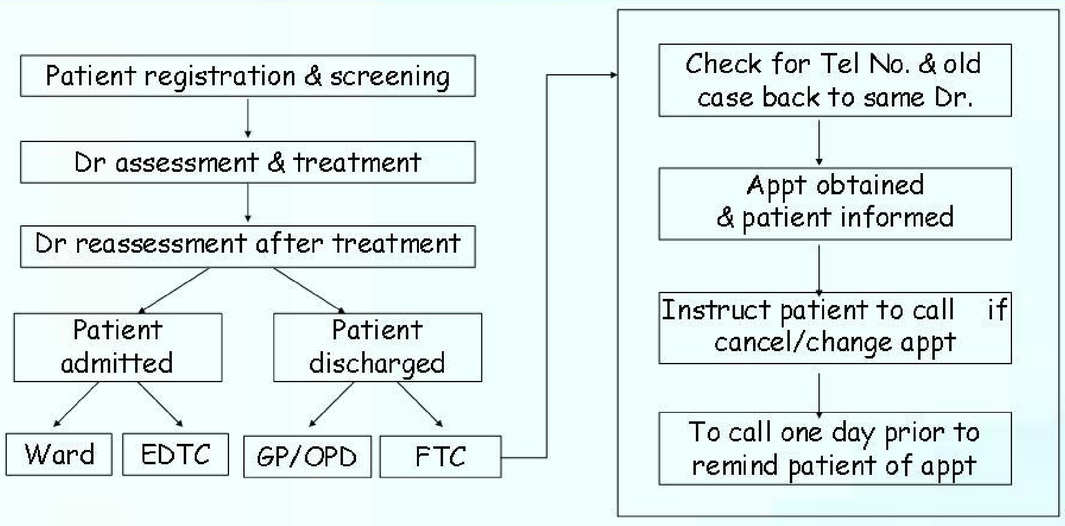

Cause & Effect Diagram

Brainstorm, survey and data analysis (from April to August 07) done to find the causes for the problem

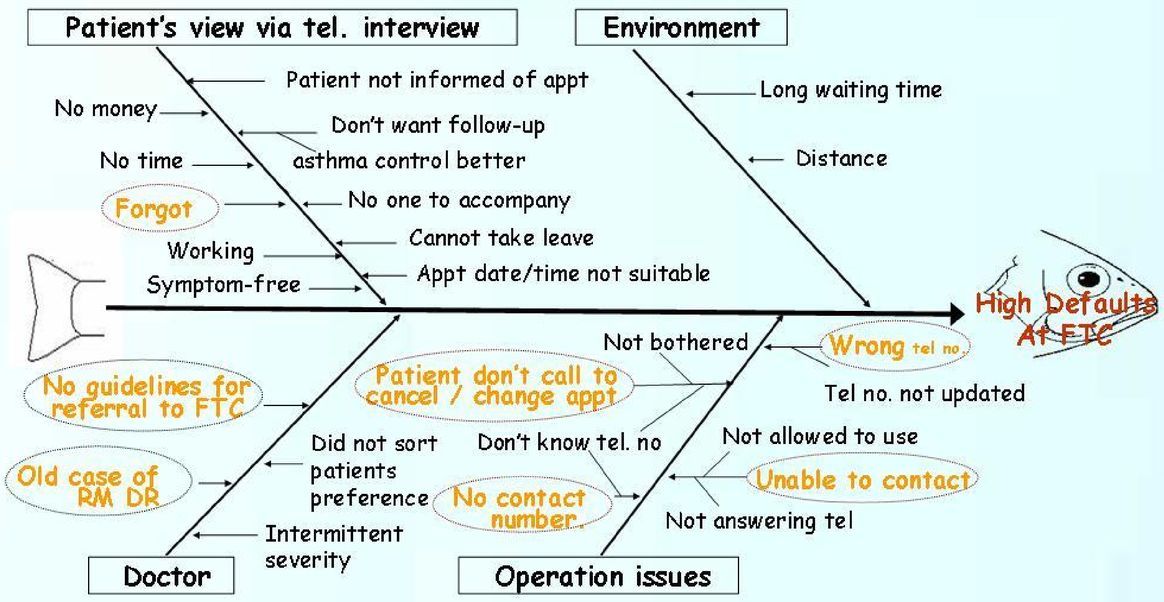

Pareto Chart

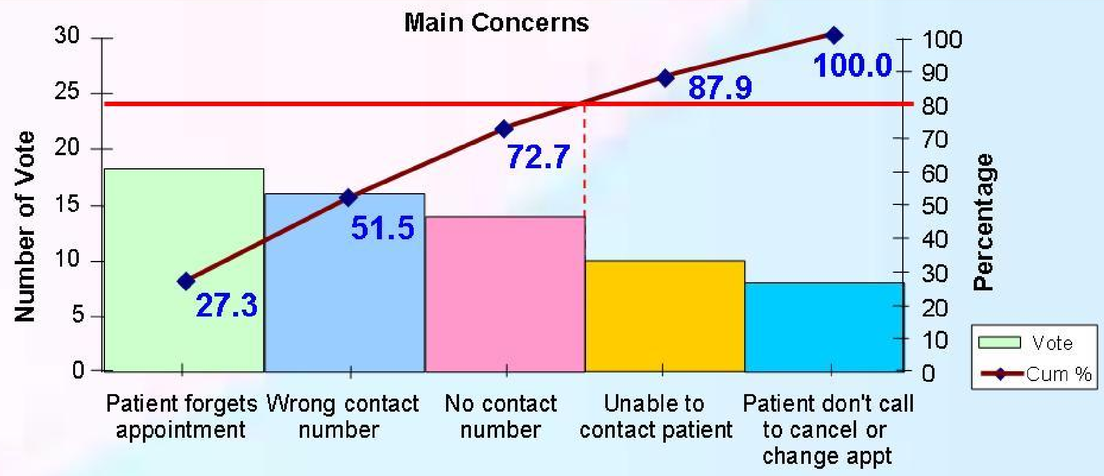

Interventions and Results

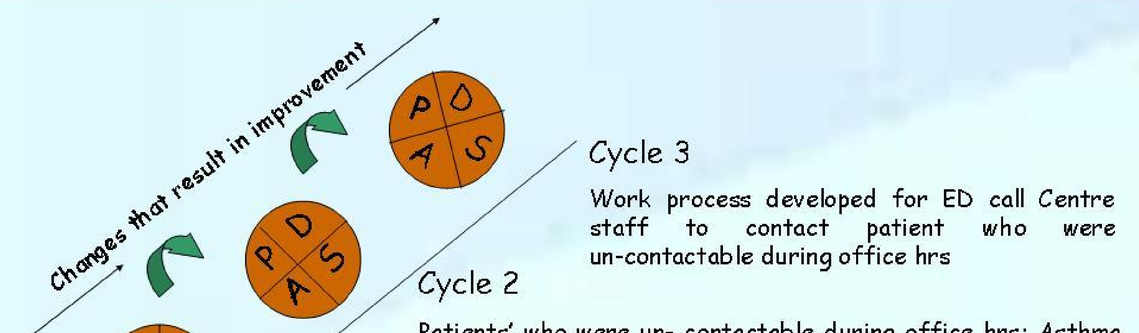

Default rates at FTC in 2008-2009

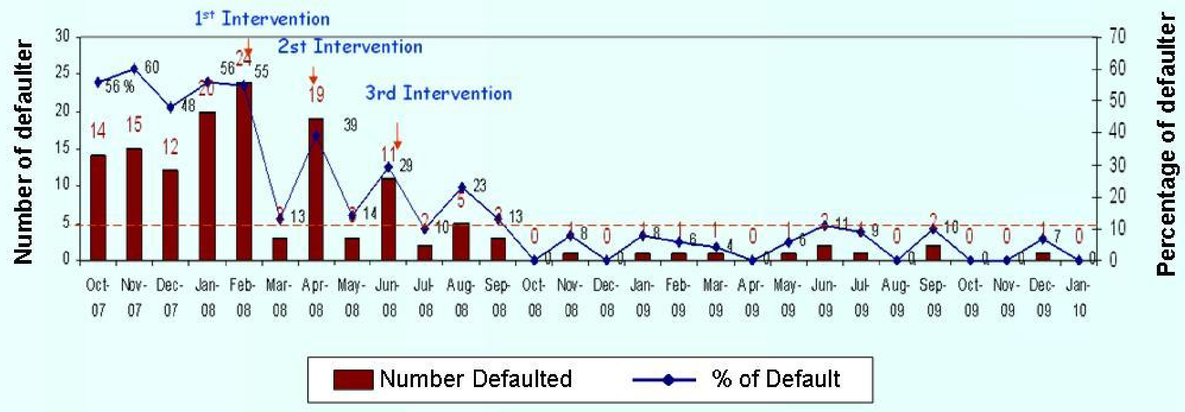

Health Care Utilization and Cost

Variables	3 month prior FTC Visits	3 month post FTC Visits	P value
Mean No. of ED Visits	1.23 (0 -10)	0.41 (0 – 28)	0.001
Mean No. of Hospitalization	0.27 (0 – 2)	0.04 (0 – 2)	0.001
Mean Cost of ED Visits	$211 (IQR $135.8 - $235.73)	$501.5 (IQR $158.5 - $487.6)	0.51
Mean Cost of Hospitalization	$489.1 (IQR $295.7 - $516.9)	$1028.6 (IQR $520.6 - $1142.8)	0.25

Strategies for Sustaining

- Continual measurement of default rates
- Target on other areas that affect frequent ED visits (i.e. cancellation of appointment).

Lessons Learned

- The project focus on the whole process of increasing the use of appropriate care delivery, to improve patient outcome therefore we learn the need to:
  - Work as a team to integrate asthma care & connect the dots…
  - Have Effective communication at all levels
  - Always keep the patient in mind
- Leadership commitment:- "Accountability for making improvement happen".

Strategies for Spreading

- Share the finding with all chronic disease management program across Hospital
- Publish the results in a quality improvement journal.

Acknowledgment

The project team members thank Mr. Yeo Y H from finance and Mr. Arul E from Clinical Research Unit for their assistance.

LEAD ON THE PLATE

LACK OF EFFICIENT REGULATION TO STOP THE RELEASE OF TOXIC EFFLUENTS INTO WATER BODIES IS ONE OF THE REASONS WHY HEAVY METALS ENTER THE FOOD CHAIN

COMPILED BY
VIDYA VENKAT

Sources of Lead

Lead (Pb):
Lead acid batteries, paints, e-waste, smelting operations, coal- based thermal power plants, ceramics, bangle industry

How can lead affect adults?

The effects of lead are the same whether it enters the body through breathing or swallowing. Long-term, and high-level exposure of adults to lead can cause brain and kidney damage.

How can lead affect children?

Children are more vulnerable to lead poisoning than adults because their nervous systems are still developing. Children are also more sensitive to the effects of lead than adults. Even at low levels of exposure, lead can affect behavior and growth.

How can I be exposed to lead?

Lead enters your body each time you inhale leaded dust or fumes, or swallow something that contains lead. Exposure to lead may occur in several ways:

- **Working in jobs where lead is used.**
- **Eating foods or drinking water that contain lead.**
- **Spending time in areas with deteriorating lead-based paint.**
- **Using medicines that contain lead.**

Data of CPCB show that Gujarat, Maharashtra and Andhra Pradesh contribute to 80% of hazardous waste (including heavy metals) in India.

Is there a way to reduce a high blood lead level?

Apart from avoiding exposure to lead, there is medication that helps remove lead from the body

Major heavy metal contaminated sites in India

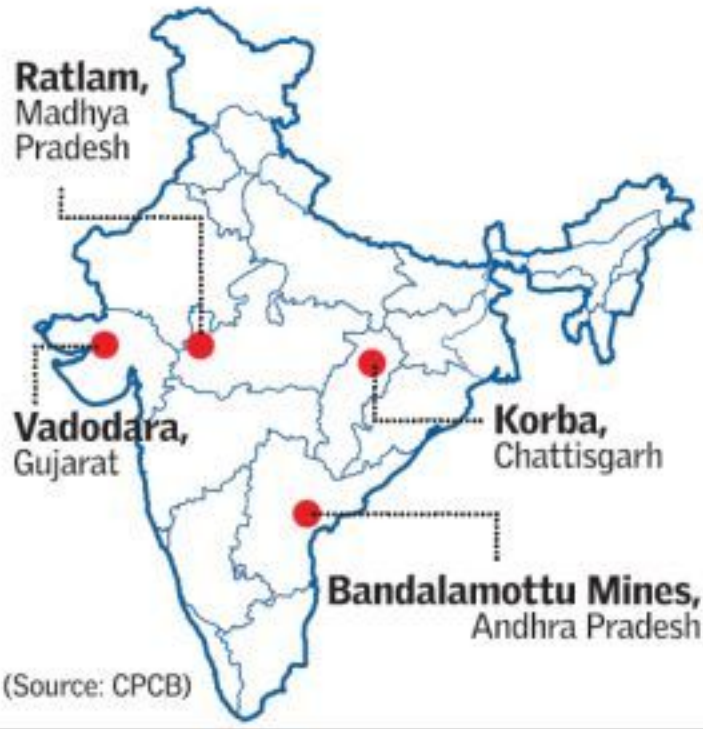

(Source: CPCB)

How biological magnification happens:

Food safety officials say that the source of lead contamination in Maggi is external

1. Heavy metal contaminated effluents and waste enter water bodies, like rivers
2. This river water is used to irrigate farm fields
3. Food grown in farm fields absorbs heavy metals
4. Effluents enter food processed through them
5. This food is then consumed. Metal concentration increases as it moves up the food chain